



TITLE:

# Single-Conductor Transmission-Line Model for Bent Wire Structures

AUTHOR(S):

Tashiro, Daiki; Sameshima, Kana; Hisakado, Takashi; Islam, A. K. M. Mahfuzul; Wada, Osami

---

CITATION:

Tashiro, Daiki ...[et al]. Single-Conductor Transmission-Line Model for Bent Wire Structures. IEEE Transactions on Electromagnetic Compatibility 2023, 65(5): 1432-1445

ISSUE DATE:

2023-10


URL:

<http://hdl.handle.net/2433/285573>

RIGHT:

This work is licensed under a Creative Commons Attribution 4.0 License.

# Single-Conductor Transmission-Line Model for Bent Wire Structures

Daiki Tashiro , *Member, IEEE*, Kana Sameshima, Takashi Hisakado , *Member, IEEE*,  
A. K. M. Mahfuzul Islam , *Member, IEEE*, and Osami Wada , *Member, IEEE*

**Abstract**—A bend in a single-conductor line is a primary cause of radiation associated with the antenna mode; conversely, the radiation is fed back, resulting in attenuation and distortion of the current waveform. Despite being a fundamental phenomenon, its dynamics have not been sufficiently characterized. Therefore, this study presents a single-conductor transmission-line model for bent wire structures comprising multiple straight elements by using the local variables of charge per-unit-length and current along a thin conductor. The proposed model is validated over a wide frequency range using the method of moments. The total charge and current distributions that an external field induces on a bent structure are classified into three components: the scattering source distribution, traveling wave corresponding to the Sommerfeld mode, and radiation reaction. These components suggest an overall field-line coupling process: initially, an external electromagnetic field induces a scattering current in the structure, which in turn drives traveling and radiation-reaction currents at the ends, resulting in propagation along the line accompanied by radiation losses. The presented model is advantageous for designing electromagnetic phenomena corresponding to antennas and metamaterials and for addressing electromagnetic interference problems using passive circuit elements. A case study that makes use of the precise and descriptive model is included to predict the field emissions associated with the antenna mode around a bend.

**Index Terms**—Antenna mode, bent wire, common mode, radiation loss, resonance, single-conductor transmission line, surface wave.

## I. INTRODUCTION

IN ELECTROMAGNETIC compatibility (EMC)/electromagnetic interference (EMI) issues concerning transmission lines (TLs), propagating modes with some explicit return paths (which are described by the classical TL theory [1]) are converted to the antenna mode, which refers to the source distribution without return current in the proximity [2], [3],

Manuscript received 7 February 2023; revised 25 May 2023; accepted 21 June 2023. Date of publication 13 July 2023; date of current version 13 October 2023. This work was supported by Grants-in-Aid for Scientific Research under Grant 18K04139 and Grant 22K04103. (Corresponding author: Daiki Tashiro.)

Daiki Tashiro is with the Central Research Institute of Electric Power Industry, Yokosuka 240-0196, Japan (e-mail: tashiro3754@criepi.denken.or.jp).

Kana Sameshima, Takashi Hisakado, and A. K. M. Mahfuzul Islam are with the Department of Electrical Engineering, Graduate School of Engineering, Kyoto University, Kyoto 615-8510, Japan (e-mail: kana.ett.1105@gmail.com; hisakado.takashi.7x@kyoto-u.ac.jp; islam.akmmahfuzul.3w@kyoto-u.ac.jp).

Osami Wada is with the Center for Future Communications Research, Nagoya Institute of Technology, Nagoya 466-8555, Japan (e-mail: wada@kuee.kyoto-u.ac.jp).

Color versions of one or more figures in this article are available at <https://doi.org/10.1109/TEMC.2023.3290844>.

Digital Object Identifier 10.1109/TEMC.2023.3290844

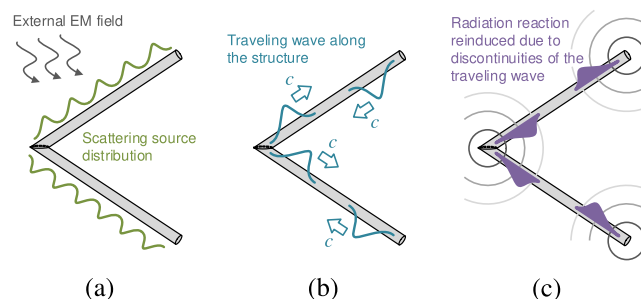


Fig. 1. Conceptual schematic for three charge/current components of the single-conductor TL theory for a bent wire structure. (a) Scattering. (b) Traveling. (c) Radiation reaction.

further generating electromagnetic (EM) emissions; conversely, from the perspective of immunity, the external EM field first induces the antenna mode, which in turn is converted into internal propagation modes. These processes are both mediated via the antenna mode; hence, understanding its dynamics is a fundamental pursuit [2], [3], [4], [5], [6], [7].

Taking appropriate measures without characterizing the entire mechanism of the antenna-mode current generation, propagation with distortion, and associated radiation losses is difficult. In particular, while radiation characteristics largely depend on the geometry of the conductor structure or charge/current distributions, they feed back as a loss on the charge/current itself, which has not been sufficiently described. In this regard, studies have focused on appropriately correlating radiation with the geometric features of wire structures such as the dimension and topology (e.g., [8], [9], [10], [11], [12]). Although challenges remain in simply incorporating radiation losses in the circuit paradigm; a model that explicitly associates the radiation with the dynamics of the current waveform is required. To focus on the antenna mode, it is useful to choose structures without a return path from the onset of modeling. Consequently, the discussion of the particular topic is also simplified, facilitating further studies on mechanisms that are peculiar to the antenna mode, namely, the interaction between sources and fields.

Propagation and scattering problems in infinite-length straight single conductors have been extensively studied [13], [14]. In the case of an infinite single wire, the total induced current can be separated into components that undergo different dynamics, the Sommerfeld-Goubau mode and the continuous radiation spectrum [15]. Since this complete approach assumes an infinite length line, it does not consider the radiation loss or resonance as

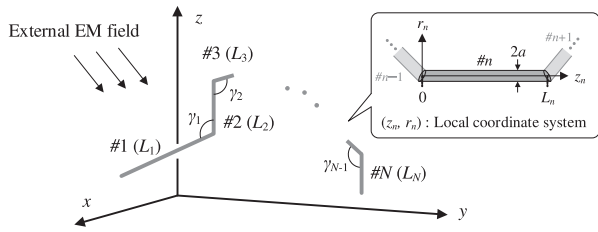


Fig. 2. Example of a single-conductor line structure comprising  $N$  straight units with arbitrary bending angles and unit lengths.  $\#n$  refers to each straight unit with length  $L_n$ .

longitudinal dynamics, as observed in the case of a finite-length wire, owing to the discontinuities at the wire ends [16], [17], [18]. This mechanism is explicitly considered in a TL model for a straight single conductor [19], and it is based on the motion of the traveling wave and the incorporation of a radiation reaction via a self-inducing electric field (E-field) caused by a discontinuity in the traveling wave.

A bend affects both EM emission and current propagation characteristics owing to radiation losses [8], [20], [21], [22], [23], [24]. In the classical electrodynamics, the aforementioned phenomenon can be viewed as the traveling wave experiencing an abrupt change in the propagation direction at the bending points, which is closely associated with radiation [25]. Therefore, extending the model [19] to bent wire structures is appropriate for addressing this topic. Fig. 1 illustrates a conceptual schematic of this extension.

Based on our previous study [19], this study presents a dynamic model for field-line coupling in bent single-conductor line structures, as depicted in Fig. 2. The presented model illustrates the complete antenna mode dynamics, in which the scattering current is induced in response to an external EM field, which in turn drives the traveling and radiation-reaction components that yield the current waveform along the conductor. Based on this decomposition, the proposed model offers the advantage of appropriately classifying the field-line coupling into contributions from individual geometric parameters, including the incident angle and polarization of the external field, bending angles, and lengths of the straight units in a bent wire structure. The effect of the bend is explained using a two-step process in which the traveling wave generates an electromotive-force field with explicit bending-angle dependence, which in turn induces a radiation-reaction current; the interrelationship between the traveling and radiation reaction can be used to explain the resonance, which depends on the geometry of a bent wire structure, such as bending angles and the position of a bend. Owing to these features, the proposed method is expected to be leveraged as a model for the antenna mode and also for the design of EM phenomena using complicated thin-wire structures. Moreover, the degree of freedom in the arrangement of wire structures is increased in the proposed model, therefore, owing to the additional degree of freedom of placement by extending to a bent structure, the applicability to fields such as research in metamaterial and plasmonics is greatly improved [26], [27], [28]. Notably, the presented model is not aimed at evaluating the performances of TLs concerning nonradiating internal propagation modes (such

as a differential mode, or a common mode that has other return paths), primarily because the model does not include return conductors as mentioned earlier.

The rest of this article is organized as follows. The finite-length single-conductor TL equation for each straight unit of a bent structure is described in Section II. A physical sketch of the E-field is developed, which is generated by a finite-length traveling wave at a wire end and reinduces the radiation reaction. Subsequently, a TL equation for a bent single-conductor line structure is formulated by considering the continuity condition between straight units. Section III validates the proposed model by utilizing the method of moments (MoM) over a wide frequency range. In Section IV, the dynamics of the field-line coupling phenomenon based on the charge/current-based components of the traveling wave, radiation reaction, and scattering are explained using the presented model. This section includes a case study to predict the field emissions around a bend owing to the antenna mode. Finally, Section V concludes this article.

## II. TL EQUATION OF A BENT SINGLE-CONDUCTOR LINE STRUCTURE

Fig. 2 illustrates an example of a wire structure comprising  $N$  straight single-conductor lines, as discussed in this article. The excitation is assumed to be time-harmonic with  $e^{j\omega t}$ . Each straight part is hereafter referred to as a “unit.” For a simple representation, we label these units as  $\#1, \dots, \#N$  in the order of their arrangement. The length of unit  $\#n$  is  $L_n$ , and the local cylindrical coordinates  $(z_n, r_n)$  are assigned such that the ends of  $\#n$  are  $z_n = 0$  and  $z_n = L_n$ . The radius of each unit is  $a$  [m], which is assumed to be sufficiently small compared to both the free-space wavelength,  $\lambda$ , and the unit length,  $L_n$ , for applying the thin-wire approximation.  $\gamma_{n-1}$  refers to the bending angle between the adjacent units  $\#n - 1$  and  $\#n$ . The variables in the local coordinate system are denoted by the subscript of the unit number,  $n$ .

### A. Single-Conductor TL Equation in the Local Coordinates

The per-unit-length (pul) charge,  $Q_n(z_n)$  [C/m], and current,  $I_n(z_n)$  [A], on a unit,  $\#n$ , are governed by a telegraph equation in the local coordinate system, expressed as

$$\frac{d}{dz_n} \begin{bmatrix} cQ_n(z_n) \\ I_n(z_n) \end{bmatrix} = \begin{bmatrix} 0 & -jk \\ -jk & 0 \end{bmatrix} \begin{bmatrix} cQ_n(z_n) \\ I_n(z_n) \end{bmatrix} + \begin{bmatrix} \sum_i \frac{j\hat{\chi}(k_i)}{Z_0} \hat{E}_n(k_i) e^{-jk_i z_n} \\ 0 \end{bmatrix} \quad (1)$$

where  $c$ ,  $k$ , and  $Z_0$  denote the speed of light, the angular wavenumber, and the characteristic impedance of free space, respectively [19]. Currently, for the ends  $z_n = 0, L_n$  can be either open-circuited or connected to another unit. In the non-homogeneous term,  $E_n(z_n) = \sum_i \hat{E}_n(k_i) e^{-jk_i z_n}$  denotes the tangential component of the total incident E-field at the surface of the unit.  $\hat{\chi}(k_i)$  denotes the induction coefficient as a function of angular wavenumber. In this study, the hatted variable denotes the wavenumber domain expression of a phasor. Notably, this

field is the summation of the external field, fields of self and mutual interaction, and field owing to the finite-length effect. The nonhomogeneous term in (1) is expressed using the inverse-Fourier-transformed product of the Fourier coefficient of the induced E-field and the wavenumber-dependent coefficients. Hence, the number of terms of the sum must be sufficiently large to approximate the distribution of the induced E-field.

Equation (1) differs only in terms of the excitation field  $E_n$  from the single-unit case ( $N = 1$ ) introduced in the literature [19]. Mutual coupling effects are included in  $E_n$  to incorporate additional fields arising from the multiple-unit structure.

For unit  $\#n$ , the total source variables  $cQ_n$  and  $I_n$  are expressed similarly by utilizing the components as the single-unit case, as follows:

$$cQ_n(z_n) = cQ_{f,n}(0)e^{-jkz_n} + cQ_{b,n}(L_n)e^{jk(z_n-L_n)} + cQ_{re,n}(z_n) + cQ_{sc,n}(z_n), \quad (2)$$

$$I_n(z_n) = I_{f,n}(0)e^{-jkz_n} + I_{b,n}(L_n)e^{jk(z_n-L_n)} + I_{re,n}(z_n) + I_{sc,n}(z_n). \quad (3)$$

In the aforementioned equations, the indices  $f$  and  $b$  refer to the forward- and backward-traveling waves, respectively, where  $cQ_{f,n}(z) = I_{f,n}(z)$  and  $cQ_{b,n}(z) = -I_{b,n}(z)$ . These correspond to the source distributions that accompany the Sommerfeld principal wave in the infinite-length wire but are truncated by the finite unit length  $L_n$ . In this model, the discontinuities in the structure are directly reflected in the discontinuities in the traveling wave. Notably, the total pul charge/current ( $cQ_n$ ,  $I_n$ ) corresponds to the antenna mode [2], [3], which also comprises the traveling wave corresponding to the Sommerfeld mode in the infinite length line. ( $cQ_{re,n}$ ,  $I_{re,n}$ ) denotes the radiation reaction, simply called the reaction, which is induced by the E-field owing to the discontinuities of the traveling wave. ( $cQ_{sc,n}$ ,  $I_{sc,n}$ ) is the scattering source in response to an external field. In (2) and (3), reaction and scattering components for a given unit  $\#n$  contain induction from the considered units  $\#1 - \#N$ . For convenience in formulating bent wire structures, the equations provided for the respective units, including mutual interactions, can be combined in a matrix form, as explained in Appendix A.

The following section focuses on the refined expression of the radiation-loss effect of the proposed TL-based model. If the reinduction on the units is not considered presently, the self-inducing E-field produced by a discontinuity of the forward-traveling wave at the  $z_n = L_n$  side end spreads spherically from the end, as depicted in Fig. 3. As demonstrated by (45) in Appendix B, the longitudinal component of the E-field opposes the vector representing the difference in velocity of the traveling wave for the positive pul charge. For example, if the phase of the forward-traveling pul charge is positive at  $z_n = L_n$ , the resulting longitudinal component of the E-field points in the  $+z_n$  direction with retardation by the speed of light. Although the traveling wave and reinduced radiation reaction are treated separately in the model, the longitudinal component of the E-field has the same propagation velocity along the line as the traveling wave, which induces a radiation reaction current that nullifies a portion

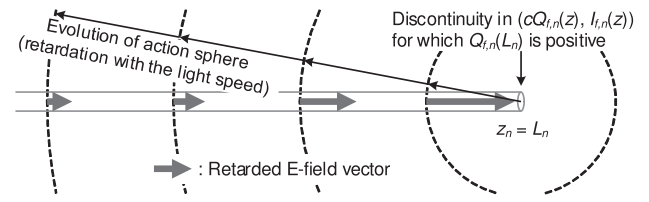


Fig. 3. Self-inducing E-field resulting from a discontinuity of the forward wave at  $z_n = L_n$  side end. The field is retarded from the end at the speed of light  $c$  and its amplitude decays as the inverse of its distance from the end.

of the traveling wave. This nullification represents radiation loss, which is crucial for representing the overall dynamics.

### B. Continuity Condition and the Single-Conductor TL Equation in the Coordinate Along the Bent Structure

As presented in this section, a TL equation is formulated for a bent wire structure that cascades  $N$  units. In the presented formulation, no restriction is imposed on the number of units, lengths of respective units, and the respective bending angles.

To obtain a continuity condition at a bending point similar to the classical TL theory [1], a circuit constant that corresponds to the characteristic impedance in the classical theory needs to be introduced, primarily because the presented TL equation utilizes the pul charge as a propagating quantity instead of the conventional “line voltage” reported in the literature [1], which will no longer be suitable for use in single-conductor line structures. The corresponding parameter is the ratio of “the product of light speed and the pul charge” to the current of the forward-traveling wave

$$cQ_{f,n}/I_{f,n} = 1 \text{ (dimensionless)}. \quad (4)$$

This ratio is invariant as long as the respective units are loss-free because the homogeneous system of (1) represents the asymptotic behavior of the principal wave in  $\sigma \rightarrow \infty$  case for wire conductivity  $\sigma$ <sup>1</sup>. Therefore, the perfect transmission condition applies to the traveling wave at the respective connection points, as follows:

$$I_{f,n}(0) = I_{f,n-1}(L_{n-1}), \quad I_{b,n}(0) = I_{b,n-1}(L_{n-1}) \quad (5)$$

for  $n = 2, \dots, N$ , where the pul charges of forward and backward waves are incidentally continuous. The condition (5) is validated by considering that the homogeneous part of the presented TL equation is based on the principal wave propagating in an infinite-length line, whose ratio of pul charge to current is constant. Notably, the EM field structure associated with the “traveling wave” expressed by the local source variables on a finite-length line is different from that of the “principal wave” on an infinite-length line. Generally, the circuit-concept approach, which assumes combining simple elements [1] does not confirm with the EM field-based principal mode propagation

<sup>1</sup>For a single-conductor line with a loss of conductivity, the propagation constant is different from the real number  $k$  and takes a complex value [15]. From the perspective of the presented theory, reflection may arise owing to mismatches in this context; however, it will be of a greater practical significance for a wire structure with branches.

formulation. Novel methods have been reported for introducing circuit parameters for a single-conductor line in terms of the EM field associated with the principal mode (see, e.g., [29], [30]). However, such methods cannot be applied to bent single-conductor line structures. This is because the principal mode inherently involves the problem of an unbound cross-section, whereas, in bent structures, nonuniform phenomena arise from the bending points, as described later in this section. While the EM field-based approach is crucial because the requirement for the existence of the Sommerfeld mode is closely related to the boundary-value problem on the surface of a conductor, it is more effective to employ the source-based approach for addressing the complete dynamics in finitely sized wire structures.

To treat a bent wire structure cascaded by straight units in the TL equation, a 1-D coordinate,  $\zeta$ , is introduced, which follows the entire path of the bent structure as shown as follows:

$$\zeta = \begin{cases} z_1 & (n = 1) \\ z_n + \sum_{\nu=1}^{n-1} L_\nu & (n = 2, \dots, N) \end{cases} \quad (6)$$

where the total length of the structure is

$$\bar{L} = \sum_{n=1}^N L_n. \quad (7)$$

In the following, the variables in the  $\zeta$ -coordinate are denoted by bars. The current in this coordinate  $\bar{I}(\zeta)$  is defined as follows:

$$\bar{I}(\zeta) \equiv \begin{cases} I_1(z_1) & 0 \leq \zeta \leq L_1 \\ I_n(z_n) & \sum_{\nu=1}^{n-1} L_\nu \leq \zeta \leq \sum_{\nu=1}^n L_\nu, \quad 2 \leq n \leq N \end{cases} \quad (8)$$

To address the aforementioned manipulations, an operator,  $\mathcal{C}[\cdot]$ , is introduced, which combines a quantity expressed in the respective local coordinates  $z_1, \dots, z_n$  into the  $\zeta$ -coordinate, by expressing (8) as

$$\bar{I}(\zeta) \equiv \mathcal{C}[\mathbf{I}]. \quad (9)$$

By using this expression, the pul charge can be expressed as

$$\bar{Q}(\zeta) \equiv \mathcal{C}[\mathbf{Q}]. \quad (10)$$

A similar relation holds true for the respective components of (9) and (10). The incident field in this coordinate,  $\bar{E}(\zeta)$ , is expressed in the same manner as

$$\bar{E}(\zeta) \equiv \mathcal{C}[\mathbf{E}]. \quad (11)$$

In practice, the distribution in the  $\zeta$ -coordinate of reaction and scattering components are obtained via the inverse Fourier transform of their wavenumber spectra. Because  $\mathbf{E}$  for an  $N$ -unit structure originates in its wavenumber domain expression, (11) is expressed for a simple representation as follows:

$$\bar{E}(\zeta) = \mathcal{C}[\mathcal{F}^{-1}[\hat{\mathbf{E}}]] \quad (12)$$

in which

$$\hat{\mathbf{E}} \equiv \left[ \hat{\mathbf{E}}(k_{-M}) \quad \dots \quad \hat{\mathbf{E}}(k_M) \right], \quad k_i = \frac{2\pi i}{\bar{L}}. \quad (13)$$

In practice, the combination of operations,  $\mathcal{C}[\mathcal{F}^{-1}[\cdot]]$  is equivalent to the inverse Fourier transform in the  $\zeta$ -coordinate. For the

first time, the basis of a Fourier series is determined by the total length  $\bar{L}$  [31]. As the  $n$ th row of  $\hat{\mathbf{E}}$  corresponds to the Fourier series of the unit  $\#n$ , the inverse spatial Fourier transform is applied to each row (i.e., for each unit). Subsequently, the obtained  $\bar{E}(\zeta)$  is expanded in the wavenumber domain as follows:

$$\bar{E}(\zeta) = \sum_i \hat{E}(k_i) e^{-jk_i \zeta}. \quad (14)$$

Thus, the Fourier series of the external field is expressed as

$$\bar{E}_{\text{ex}}(\zeta) = \sum_i \hat{E}_{\text{ex}}(k_i) e^{-jk_i \zeta}. \quad (15)$$

Using (5),  $\mathbf{I}_f(\mathbf{0})$  and  $\mathbf{I}_b(\mathbf{L})$  introduced in (39) are expressed with the open-end values,  $\bar{I}_f(0)$  and  $\bar{I}_b(\bar{L})$ , as

$$\mathbf{I}_f(\mathbf{0}) = \bar{I}_f(0) \begin{bmatrix} 1 \\ e^{-jkL_1} \\ \vdots \\ e^{-jk \sum_{n=1}^{N-1} L_n} \end{bmatrix}, \quad \mathbf{I}_b(\mathbf{L}) = \bar{I}_b(\bar{L}) \begin{bmatrix} e^{-jk \sum_{n=2}^N L_n} \\ \vdots \\ e^{-jkL_N} \\ 1 \end{bmatrix}. \quad (16)$$

Therefore,  $\bar{E}_f(\zeta)$  and  $\bar{E}_b(\zeta)$  are expressed using  $\bar{I}_f(0)$  and  $\bar{I}_b(\bar{L})$  as

$$\bar{E}_f(\zeta) = \sum_i \hat{Z}'_f(k_i) e^{-jk_i \zeta} \bar{I}_f(0) = \mathcal{C} \left[ \mathcal{F}^{-1} \left[ \hat{\mathbf{Z}}'_f \mathbf{I}_f(\mathbf{0}) \right] \right] \quad (17)$$

$$\bar{E}_b(\zeta) = \sum_i \hat{Z}'_b(k_i) e^{-jk_i \zeta} \bar{I}_b(\bar{L}) = \mathcal{C} \left[ \mathcal{F}^{-1} \left[ \hat{\mathbf{Z}}'_b \mathbf{I}_b(\mathbf{L}) \right] \right] \quad (18)$$

and similarly, the finite-length effect for the scattering and reaction components is expressed by defining  $\hat{Z}'_j(k_i)$  as follows:

$$\sum_{i,j} \hat{Z}'_j(k_i) \hat{I}_{\text{sc}}(k_j) e^{-jk_i \zeta} \equiv \mathcal{C} \left[ \mathcal{F}^{-1} \left[ \sum_j \hat{\mathbf{Z}}'_j \hat{\mathbf{I}}_{\text{sc}}(k_j) \right] \right]. \quad (19)$$

The longitudinal component of the E-field, generated by the traveling wave  $E_{\parallel}$  [(45) and (47) produced by  $\#n$ ], serves as the driving force in the single-unit case introduced in [19], whereas in the case of a bent wire, the transversal (radial) component  $E_{\perp}$  [(46) and (48) produced by  $\#n$ ] also contributes as a mutual effect between the straight units in a bent structure. From a physical perspective, the difference between the E-field components,  $E_{\parallel}$  and  $E_{\perp}$ , is of great relevance.

1)  $E_{\parallel}$  is generated by discontinuities in the traveling wave, which is weighted near the end of the emitting-side unit. Importantly,  $E_{\parallel}$  should not be confused with the longitudinal E-field of the transverse magnetic Sommerfeld mode supported by a lossy single conductor [13]. In a bent wire structure, this field component is generated at

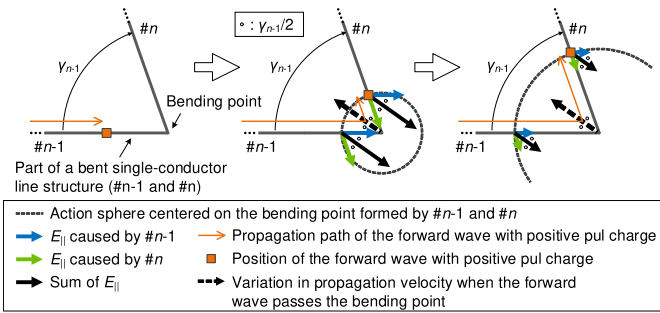


Fig. 4. Time evolution of the longitudinal E-field component  $E_{\parallel}$  for each unit of  $\#n - 1$  and  $\#n$  generated by the forward wave propagating through these units. The vectors in blue and green represent the field component owing to  $\#n - 1$  and  $\#n$ , respectively, and solid vectors in black represent their sum. The direction of these sum vectors points in the direction opposite to the vector representing the change in velocity of the forward-traveling wave at the bending point, which is denoted by the dashed vector in black. The vector sum of  $E_{\parallel}$  denotes an extension of the field vectors originating from an end which is shown in Fig. 3.

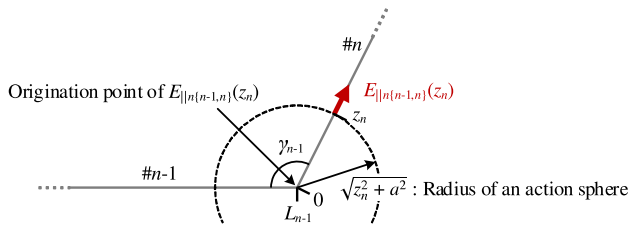


Fig. 5. Evaluation of the tangential component of the sum of E-field  $E_{\parallel}$  (owing to the forward and backward waves) originating from the bending point.

the bending points and ends.  $E_{\parallel}$  is illustrated in Fig. 4, which originates at the bending point owing to the forward wave propagating through  $\#n - 1$  and  $\#n$ . This field spreads with a spherical wavefront centered on the bending point, applied at the line with retardation. Qualitatively, the vector sum of  $E_{\parallel}$  produced by the forward wave discontinuity at the corner (each solid vector in black in Fig. 4) points in the opposite direction of the vector, which indicates the difference in propagation velocity as it passes the corner (the dashed vector in black), thereby extending the single-unit case illustrated in Fig. 3. From a geometrical perspective, (45) and (47) are only dependent on the free-space Green's function of distances from the ends,  $d_{0,n}$  and  $d_{L,n}$ , which indicates that these E-field vectors are identical throughout a common action sphere centered on one end (refer to each snapshot in Fig. 4). This also holds true for the sum of  $E_{\parallel}$  by the units originating from the corner, wherein its component tangential to  $\#n$  on the unit surface (refer to Fig. 5) is rendered as

$$E_{\parallel\{n-1,n\}}(z_n) = -Z_0 G\left(\sqrt{z_n^2 + a^2}\right) cQ_{\text{tr},n}(0)(1 + \cos \gamma_{n-1}) \quad (20)$$

where  $G(d)$  denotes the free-space retarded Green's function of distance  $d$ , as defined in (50) in Appendix B. The suffix  $\{n-1,n\}$  indicates the origin of the field, which in the case of Fig. 5 is the corner formed by  $\#n - 1$  and  $\#n$ .

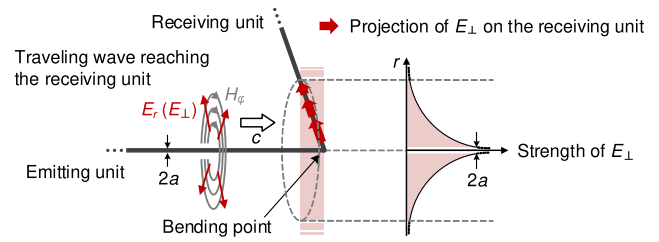


Fig. 6. Conceptual diagram for induction through the transverse field component  $E_{\perp}$ , which is generated by the traveling wave reaching the bending point. The field component is cylindrically symmetric, and its amplitude tends to decrease by the function  $1/r$ .

Equation (20) yields an optimal qualitative and quantitative description of the reinducing E-field in terms of its dependence on geometry and the phase condition of the standing wave. The two different properties of 1) bending angle  $\gamma_{n-1}$  [the size of (20) increases monotonically as the bend is rendered increasingly acute] and 2) the phase condition of the traveling wave's pul charge at the bending point [for example, (20) disappears as the bending point is at the node of  $c\bar{Q}_{\text{tr}}$  or as the antinode of  $\bar{I}_{\text{tr}}$  are decomposed owing to certain factors.

- 2)  $E_{\perp}$  can be understood as the component associated with the traveling wave; therefore, the induction through this component is closely related to the transverse dimensions of the Sommerfeld mode. Fig. 6 illustrates this in the form of a conceptual diagram. A part of the receiving-side unit is directly excited as it is “immersed” in the traveling wave propagating on the emitting-side unit, and it is not a retarded interaction that originates from an end or bending point as  $E_{\parallel}$  does. According to (46) and (48), the extent of this field component is frequency-independent and tends to decrease by the function of  $1/r$ , particularly in the case of an acute bend.

A subtle but fundamental difference exists between how the respective field components reinduce the radiation reaction<sup>2</sup> (the field structures are spherical for  $E_{\parallel}$  and cylindrical for  $E_{\perp}$ ), which will produce different dynamics around the bending points. Based on this distinction, the currents induced by the various E-field components are classified as  $\bar{I}_{\text{re}\parallel}$  and  $\bar{I}_{\text{re}\perp}$ , with  $\bar{I}_{\text{re}} \equiv \bar{I}_{\text{re}\parallel} + \bar{I}_{\text{re}\perp}$ . With respect to  $\bar{I}_{\text{re}\parallel}$ , it can be further subdivided into  $\bar{I}_{\text{re}\parallel\{1\}}$ ,  $\bar{I}_{\text{re}\parallel\{1,2\}}$ ,  $\dots$ ,  $\bar{I}_{\text{re}\parallel\{N-1,N\}}$ ,  $\bar{I}_{\text{re}\parallel\{N\}}$  because the E-fields originating from the respective ends and bending points are localized.

Equations (1)–(3), (41), and (42) are provided in the local coordinate systems and they must be reallocated in the global coordinate system defined by (6). The total TL equation as an extension of (1) can be written as

$$\frac{d}{d\zeta} \begin{bmatrix} c\bar{Q}(\zeta) \\ \bar{I}(\zeta) \end{bmatrix} = \begin{bmatrix} 0 & -jk \\ -jk & 0 \end{bmatrix} \begin{bmatrix} c\bar{Q}(\zeta) \\ \bar{I}(\zeta) \end{bmatrix}$$

<sup>2</sup>Note that it is arguable whether the induction by  $E_{\perp}$  should be called a “radiation reaction” as it does not directly reflect the discontinuity of a traveling wave as  $E_{\parallel}$  does. In this study, the induction by the E-field due to the traveling wave is referred to as the radiation reaction for convenience of classification.

$$+ \begin{bmatrix} \sum_i \frac{j\hat{\chi}(k_i)}{Z_0} \hat{E}(k_i) e^{-jk_i\zeta} \\ 0 \end{bmatrix} \quad (21)$$

and the total source variables,  $c\bar{Q}(\zeta)$  and  $\bar{I}(\zeta)$ , are expressed using the traveling, reaction, and scattering components as follows:

$$c\bar{Q}(\zeta) = c\bar{Q}_f(0)e^{-jk\zeta} + c\bar{Q}_b(\bar{L})e^{jk(\zeta-\bar{L})} + c\bar{Q}_{re}(\zeta) + c\bar{Q}_{sc}(\zeta) \quad (22)$$

$$\bar{I}(\zeta) = \bar{I}_f(0)e^{-jk\zeta} + \bar{I}_b(\bar{L})e^{jk(\zeta-\bar{L})} + \bar{I}_{re}(\zeta) + \bar{I}_{sc}(\zeta). \quad (23)$$

The nonhomogeneous solutions are expressed in a similar way as (41) and (42) in Appendix A, as follows:

$$\begin{bmatrix} c\hat{Q}_{sc}(k_i) \\ \hat{I}_{sc}(k_i) \end{bmatrix} = \frac{\hat{\chi}(k_i)}{(k^2 - k_i^2)Z_0} \begin{bmatrix} k_i \\ k \end{bmatrix} \left\{ \hat{E}_{ex}(k_i) - \sum_j \hat{Z}_j(k_i) \hat{I}_{sc}(k_j) \right\} \quad (24)$$

$$\begin{bmatrix} c\hat{Q}_{re}(k_i) \\ \hat{I}_{re}(k_i) \end{bmatrix} = \frac{\hat{\chi}(k_i)}{(k^2 - k_i^2)Z_0} \begin{bmatrix} k_i \\ k \end{bmatrix} \left\{ \hat{E}_{tr}(k_i) - \sum_j \hat{Z}_j(k_i) \hat{I}_{re}(k_j) \right\} \quad (25)$$

where  $\hat{E}_{tr}(k_i)$  denotes the re-inducing E-field due to the traveling wave, further described by

$$\hat{E}_{tr}(k_i) = \hat{Z}_f(k_i) \bar{I}_f(0) + \hat{Z}_b(k_i) \bar{I}_b(\bar{L}). \quad (26)$$

Relationship expressing the finite-length effect

$$\hat{Z}_j(k_i) = -\frac{(k^2 - k_j^2)Z_0}{k\hat{\chi}(k_j)} \delta_{ij} + \hat{Z}'_j(k_i) \quad (27)$$

and the currents as a nonhomogeneous solution are obtained using

$$\sum_j \hat{Z}'_j(k_i) \hat{I}_{sc}(k_j) = \hat{E}_{ex}(k_i) \quad (28)$$

$$\sum_j \hat{Z}'_j(k_i) \hat{I}_{re}(k_j) = \hat{E}_{tr}(k_i). \quad (29)$$

Hence, the current components in (23) are expressed with two unknowns  $\bar{I}_f(0)$  and  $\bar{I}_b(\bar{L})$ , similar to the  $N = 1$  case reported in [19], and these are determined via KCL

$$\bar{I}(0) = \bar{I}(\bar{L}) = 0. \quad (30)$$

The expression can be rewritten in terms of the traveling-wave currents at the terminals as

$$\underbrace{\begin{bmatrix} 1 + \bar{\alpha}_f & e^{-jk\bar{L}} + \bar{\alpha}_b \\ e^{-jk\bar{L}} + \bar{\alpha}_f & 1 + \bar{\alpha}_b \end{bmatrix}}_{\text{traveling + radiation reaction}} \begin{bmatrix} \bar{I}_f(0) \\ \bar{I}_b(\bar{L}) \end{bmatrix} = - \underbrace{\begin{bmatrix} \bar{I}_{sc}(0) \\ \bar{I}_{sc}(\bar{L}) \end{bmatrix}}_{\text{scattering}} \quad (31)$$

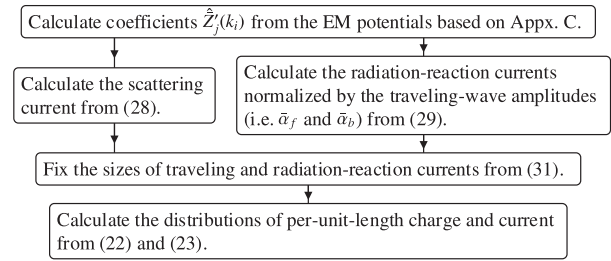


Fig. 7. Flowchart of the proposed method.

where  $\bar{\alpha}_f$  and  $\bar{\alpha}_b$  denote the radiation reaction currents for the forward and backward waves with the normalization of  $\bar{I}_f(0) = 1$  and  $\bar{I}_b(\bar{L}) = 1$ , respectively. Notably, the effect of bending angle is included in radiation-reaction  $\bar{\alpha}_f$  and  $\bar{\alpha}_b$ . In contrast to the case of  $N = 1$  [19], the structure can be asymmetric in terms of forward and backward propagation (for example, in the case of  $L_1 \neq L_2$  in an L-shaped structure); thus,  $\bar{\alpha}_f$  and  $\bar{\alpha}_b$  are not identical in general.

The flowchart of the proposed method is provided in Fig. 7. As the proposed model is closed-form by considering the radiation reaction and finite-length effects, the workflow is simple and does not involve iterative operations.

### C. Physical Interpretation

Notably, as demonstrated by (31), the internal characteristics represented by the sum of the traveling and radiation reaction and the external characteristics represented by the scattering source are only associated at the two ends  $z = 0, \bar{L}$ . Furthermore, it is evident from the above workflow that the source distributions of the traveling, radiation reaction, and scattering components are known before solving (31), except for the amplitude of the traveling wave at the ends,  $\bar{I}_f(0)$  and  $\bar{I}_b(\bar{L})$ . Therefore, the entire phenomenon can be interpreted as follows: owing to structural discontinuities, the wire-end values of a distributed scattering source drive the traveling and radiation reaction components at both ends. To ensure that the principal mode dominates the entire phenomenon, discussions on the excitation of this mode are generally concerned with either the illumination of a high-concentration EM field externally [32] or the application of efficient launching equipment [24], [33]. Furthermore, the model focuses on a similar characteristic exhibited by discontinuities in finitely sized wire structures, wherein the application of KCL to the ends (30) assumes a primary condition in the entire dynamic, which is beyond a simple continuity condition. In problematic manifestations of EMI, discontinuity is crucial as the source of antenna-mode currents in a circuit context and radiated EM fields in an antenna context.

## III. VALIDATION OF THE MODEL

The proposed model was tested against the full-wave numerical simulation based on the MoM using the FEKO software package. Although different cases, such as those involving structures with different unit lengths and the oblique incidence of excitation, have been utilized to validate the presented model,

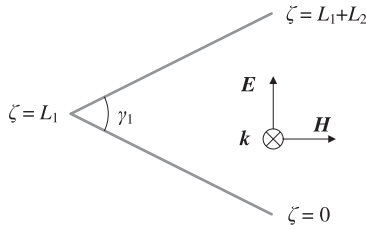


Fig. 8. In-phase excitation of an L-shaped single conductor line.

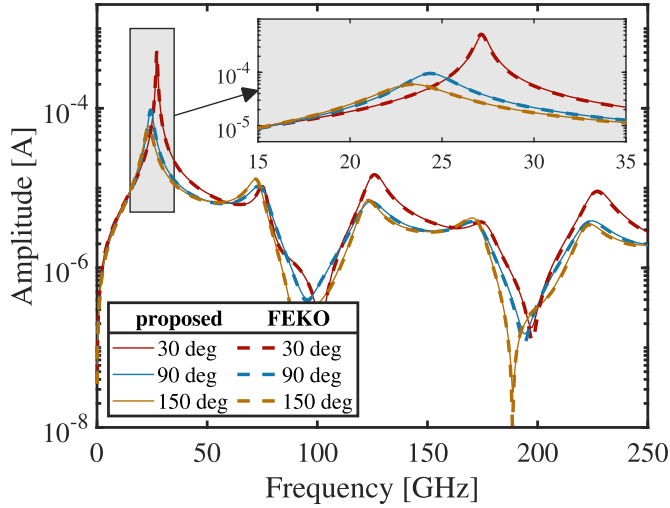


Fig. 9. Total current amplitude frequency characteristics at  $\zeta = \bar{L}/2$  (bending point) for bending angles  $\gamma_1 = 30^\circ, 90^\circ$ , and  $150^\circ$ ,  $L_1 = L_2 = 3$  mm,  $a = 15$   $\mu\text{m}$  and the excitation is normalized to  $E_{\text{ex}} = 1$ . The results of the model (solid lines) accurately reflect those obtained via the MoM (dashed lines). These results indicate that the center frequency and Q factor at each resonance vary depending on the bending angle.

a straightforward example was leveraged in this study to avoid complex phenomena.

The configuration is illustrated in Fig. 8, where the length of two straight units is the same as  $L_1 = L_2 = 3$  mm, with a wire radius  $a = 15$   $\mu\text{m}$ . Fig. 9 shows the frequency characteristics of the current amplitude at the bending point of the L-shaped structure,  $\zeta = \bar{L}/2$ , for different bending angles of  $\gamma_1 = 30^\circ, 90^\circ$  and  $150^\circ$ . To facilitate the subsequent discussions, as illustrated in Fig. 9,  $|\mathbf{E}| = 1/\sin(\gamma_1/2)$  V/m is implemented to normalize the amplitude of the field component longitudinal to the line as  $E_{\text{ex}} = 1$  V/m in response to the bending angle  $\gamma_1$ . The total currents of the proposed model were verified against those obtained via MoM for the corresponding bending angles. The characteristics corresponding to the first resonance indicate that the center frequency,  $f_c$ , deviates from the half-wavelength  $\lambda/2 \sim 25$  GHz (for example,  $f_c = 27.2$  GHz for  $\gamma_1 = 30^\circ$  and  $f_c = 23.4$  GHz for  $\gamma_1 = 150^\circ$ ), and the Q factor varies depending on  $\gamma_1$ .

#### IV. DISCUSSION

##### A. Resonant Characteristics

In this section, we examine the effects of the geometry of the wire structure on these features. Fig. 10 displays the frequency

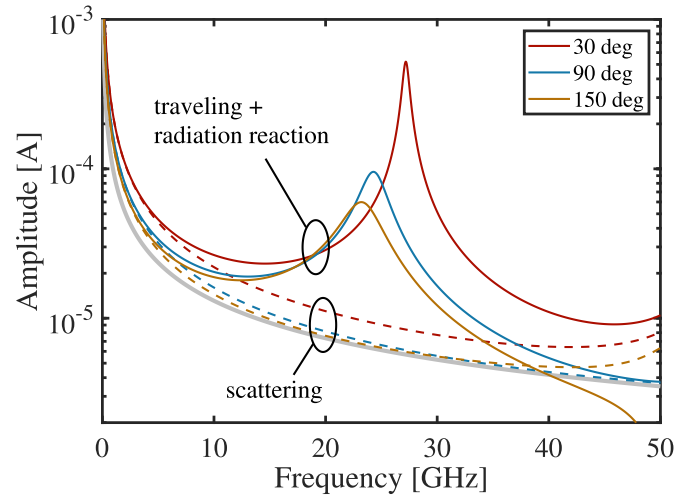


Fig. 10. Maximum current amplitude for each of “sum of traveling and radiation reaction” and “scattering” for the same configuration in Fig. 9 up to 50 GHz. The thick grey line represents the theoretical curve of the scattering current by an infinite-length line (32). For most cases, the maximum amplitudes could be obtained at the bending point.

characteristics of the current amplitude divided by the internal ( $\bar{I}_{\text{tr}} + \bar{I}_{\text{re}}$ ) and external ( $\bar{I}_{\text{sc}}$ ) components for three cases ( $\gamma_1 = 30^\circ, 90^\circ$ , and  $150^\circ$ ) in Fig. 9. It can be observed that because the traveling and radiation reaction components are standing waves with the same longitudinal wavenumber as  $k$ , the scattering component exhibits a relatively small dependence on  $\gamma_1$  and possesses a much lower frequency response than the internal current. This result implies that these components propagate along the line at the speed of light and that their characteristics change significantly depending on the ratio of  $\bar{L}$  to  $\lambda$ . Even for a bent and finite-length wire structure, the scattering component is inherited from the ideal characteristics of scattering through an infinite wire. Such a theoretical characteristic is useful as a reference for an actual scattering current to determine the entire field-line coupling mechanism. For example, the theoretical scattering current,  $\bar{I}_{\text{sc}}(z)$ , when an infinite-length wire is excited by a sinusoidal plane wave in phase with the tangential E-field  $E_{\text{ex}}$  is transformed into

$$\bar{I}_{\text{sc}}(z) = \frac{\hat{\chi}(0)E_{\text{ex}}}{kZ_0} = \frac{4E_{\text{ex}}}{kZ_0 J_0(ka)H_0^{(2)}(ka)} \quad (32)$$

where only the azimuthally symmetric term is considered for applying the thin-wire approximation [34]. Here,  $J_0(\cdot)$  and  $H_0^{(2)}(\cdot)$  refer to the Bessel function of zeroth order and the Hankel function of zeroth order and second kind, respectively. The amplitude of (32) is represented in Fig. 10, with the thick line in gray as reference. This result exemplifies the broad physical concept revealed by the presented model: the scattering component, which is relatively insensitive to frequency, first determines the fundamental characteristics of the thin wire structure as a scatterer to an external EM field, and upon this component, the traveling wave dynamics and its radiation reaction are superposed. As a perfect conductor line is excited by a quasi-static E-field in the low-frequency domain (approximately  $f = 0$  in Fig. 10), the amount of scattering current that is not required



to observe KCL by the component is enlarged. In response, the sizes of the traveling wave's current amplitude and radiation reaction current applied from both ends grow in accordance with the scattering current based on KCL, as demonstrated in Fig. 9. Hence, regardless of the frequency, the componentwise expression correctly reflects their mechanisms.

The characteristics of these three components yield insights into the contributions of radiation to the resonance of single-conductor line structures. The frequency characteristics of the maximum current amplitude for each component (the traveling and radiation reaction components are evaluated by their sum) are plotted in Fig. 10. It can be observed that the resonance condition depends largely on the inter-relationship between the traveling and radiation reaction components, with the exception of the scattering, primarily because the scattering current on the right-hand side of (31) exhibits minimal fluctuation compared to those of the other components within the resonant width.

Using the identity of  $\bar{I}_{sc}(0)$  and  $\bar{I}_{sc}(\bar{L})$  owing to the finite-length effect, the terminal values of the traveling-wave current are transformed into

$$\bar{I}_f(0) = \bar{I}_b(\bar{L}) = -\frac{\bar{I}_{sc}(0)}{K} \quad (33)$$

$$K = 1 + e^{-jk\bar{L}} + \bar{\alpha}_f + \bar{\alpha}_b. \quad (34)$$

In (34), the sum of the first two terms,  $1 + e^{-jk\bar{L}}$  denotes the value of the traveling-wave current at the terminals, and the sum of the last two terms,  $\bar{\alpha}_f + \bar{\alpha}_b$ , denotes the value of the reaction current, both under the normalization of  $\bar{I}_f(0) = 1$ . Because the scattering current, which is derived from (28) and independent of the traveling wave, is fundamentally irrelevant to the length-dependent periodicity as that of the standing wave, the shift of the resonant frequency and fluctuating Q factor observed in Fig. 9 are rendered by the interaction between the traveling and reaction components, which is reflected in  $K$ .

The frequency characteristics of  $|K|$  are illustrated in the second graph of Fig. 11 along with the current amplitude at around the first resonance for the same conditions as those corresponding to Fig. 9. The “reference” plots in Fig. 11 illustrate the results that exclude induction of the reaction currents and the finite-length effects. Consequently, their characteristics are irrelevant to the bending angle,  $\gamma_1$ , and the first resonant frequency (25 GHz) precisely matches  $c/2\bar{L}$ . The frequencies where  $|K|$  assume their minimal values (dips) at approximately 25 GHz for the respective angle  $\gamma_1$  correspond to the first resonance points (peaks) in the current amplitude illustrated in the first graph of Fig. 11. The amplitude of the traveling wave tends to be inversely proportional to that of  $K$ , where the scattering current has a relatively small reliance on the frequency within the resonance width, thereby yielding this trend. This result indicates that the reaction current,  $\bar{\alpha}_f + \bar{\alpha}_b$ , causes a change in the fundamental characteristics determined by the traveling wave  $1 + e^{-jk\bar{L}}$ , resulting in different resonant characteristics for different bending angles.

As a frequency characteristic, the dip depth of  $K$  indicates the optimal manner through which  $\bar{I}_{tr}$  and  $\bar{I}_{re}$  cancel each other at the wire ends  $\zeta = 0, \bar{L}$ . It can be observed that the

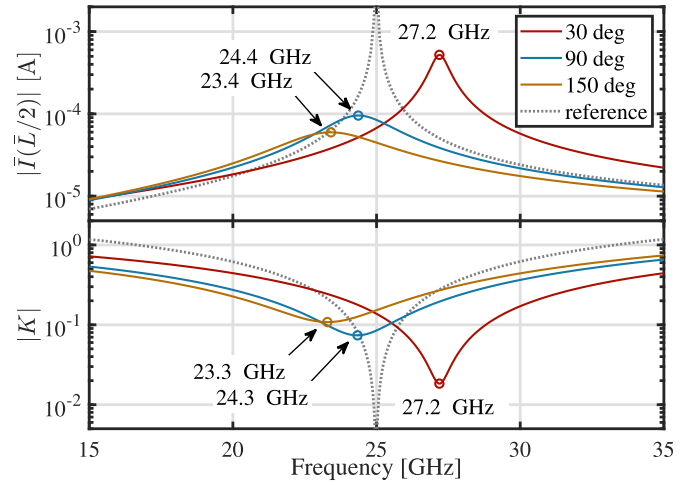


Fig. 11. Frequency characteristics of  $|\bar{I}(\bar{L}/2)|$  and  $|K|$  for the same condition as Fig. 9. The “reference” lines ignore the induction of radiation reaction currents and the finite-length effects. The dips in  $|K|$  correspond to the peaks in  $|\bar{I}(\bar{L}/2)|$ . The dotted line in gray shows the result without considering the radiation reaction and finite-length effect, which is similar to that obtained via (31) in [19].

actual resonance is yielded by the cancellation between these components at the ends of the structure. The higher Q factor of resonance indicates that the traveling and reaction currents cancel each other out more completely at the wire ends. The summed current  $K$  reduces compared to its actual amount (i.e., its peak amplitude in the distribution) at a resonant point, and the small but nondegenerated terminal value is utilized to cancel the terminal value of the scattering current. Conversely, the resonance is interpreted in the following manner: the relatively small terminal value of scattering current arises, and subsequently, this terminal value drives larger traveling and reaction currents.

Therefore, the plausible mechanism driving the entire field-line coupling interpreted based on the presented model can be explained as follows: as an instantaneous phenomenon, the scattering current is first induced in response to the external EM field, and this component in turn drives the traveling and reaction components at the wire ends, thereby generating longitudinal motion of a current wave.

### B. Effect of Bend on Induced Current

In this study, an asymmetric L-shaped structure was employed to investigate the effect of bending [for which the longitudinal part of the E-field is given by (20)]. Maintaining the total length  $\bar{L} = L_1 + L_2$ , the lengths of the two units are shifted with the length of the unbalance  $\delta$ , as depicted in Fig. 12, which is used to regulate the phase condition of the traveling wave at the bending point. The structure is symmetric when  $\delta = 0$  ( $L_1 = L_2 = \bar{L}/2$ ), and the bending point is located at a node of  $c\bar{Q}_{tr}$  (referred to as the “NQ” point); if  $\delta \neq 0$ , this parameter is asymmetric ( $L_1 = \bar{L}/2 - \delta, L_2 = \bar{L}/2 + \delta$ ), and at  $\delta = (2m - 1)\lambda/4$ , for which  $m$  is an integer, the bending point is located at the antinode of  $c\bar{Q}_{tr}$  (node of  $\bar{I}_{tr}$ , referred to as the “NI” point), where the E-field (20) strengthens by the factor  $c\bar{Q}_{tr,2}(0)$ . As  $\delta$  changes, the bending point alternates between NQ and NI conditions, as shown in Fig. 12.

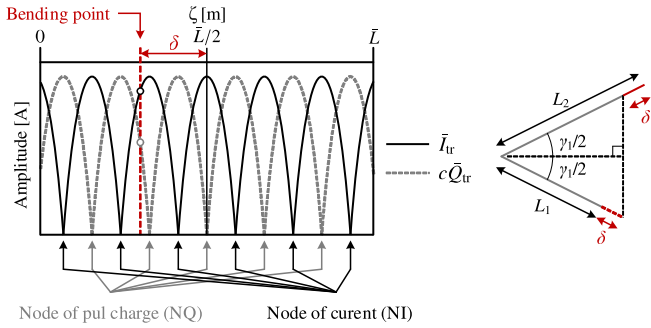


Fig. 12. Asymmetric L-shaped structure and the traveling-wave phase condition at the bending point.

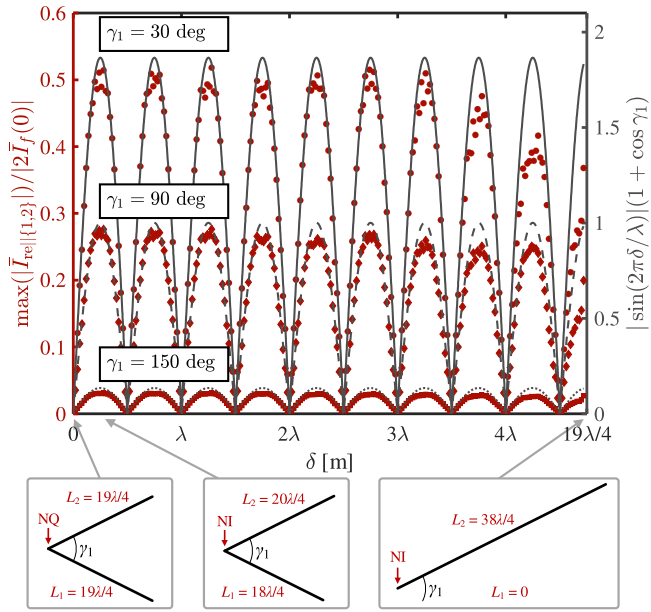


Fig. 13. Maximum amplitude of the distributed  $\bar{I}_{re||\{1,2\}}(\zeta)$  normalized by the standing wave amplitude of  $\bar{I}_{tr}$  and the function of  $\bar{E}_{||\{1,2\}}(\zeta)$  as characteristics of  $\delta$ . The function  $\sin(2\pi\delta/\lambda)$  is leveraged to imitate the phase condition of  $c\bar{Q}_{tr}$  at the bending point.

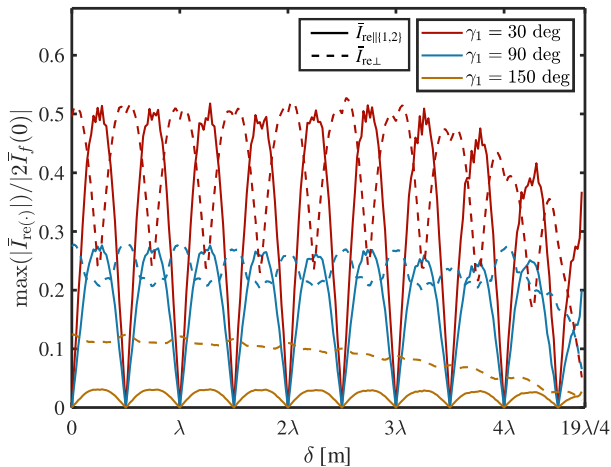


Fig. 14. Maximum amplitude of the distributed  $\bar{I}_{re||\{1,2\}}(\zeta)$  and  $\bar{I}_{re\perp}(\zeta)$  normalized by the standing wave amplitude of  $\bar{I}_{tr}$  as characteristics of  $\delta$ .

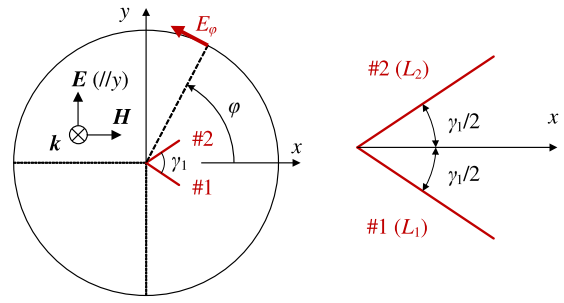


Fig. 15. Schematic of the configuration to evaluate the far-field and general-field.

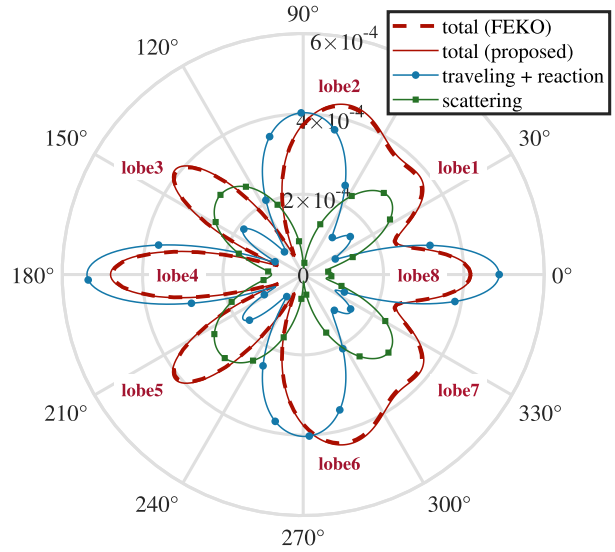


Fig. 16. Far E-field pattern  $|E_{\phi}|$  (in volts) in Fig. 15. Dominant components, which produce each lobe are listed in Table I. Owing to the difference in the far-field generation mechanism, the patterns differ between  $\bar{I}_{tr} + \bar{I}_{re}$  and  $\bar{I}_{sc}$ .

To evaluate this effect, we employed a structure with  $\bar{L} = 28.5$  mm and  $a = 5$   $\mu\text{m}$  and an exciting frequency of  $f = 100$  GHz, at which  $\bar{L} \sim 19\lambda/2$ . The effect of the bending angle was evaluated using three cases:  $\gamma_1 = 30^\circ$ ,  $90^\circ$ , and  $150^\circ$ . The maximum current amplitude of  $\bar{I}_{re||\{1,2\}}(\zeta)$  distribution as a response to  $\delta$  is plotted in Fig. 13, and the results are compared to the characteristics of the applied E-field (20). Moreover, the results indicate that while the amplitude of the induced reaction current owing to the bending point is relatively small at an obtuse bending angle, the size increases as the acuteness increases, which is closely explained by the function that imitates (20). The magnitude of the induced reaction current shifts periodically according to the phase condition of the standing wave at the bend. These results accurately explained the effect of the physical bend with the respective factors of the analytical E-field (20); however, it comes to the surface through the resulting induced reaction current. The effect is implicitly included in the reaction current and explicitly in the E-field that induces the reaction current. In addition to the reaction component resulting from  $E_{||}$  illustrated in Fig. 13, the maximum amplitude of the reaction current owing to  $E_{\perp}$  (i.e.,  $\bar{I}_{re\perp}$ ) is depicted in Fig. 14. The characteristics

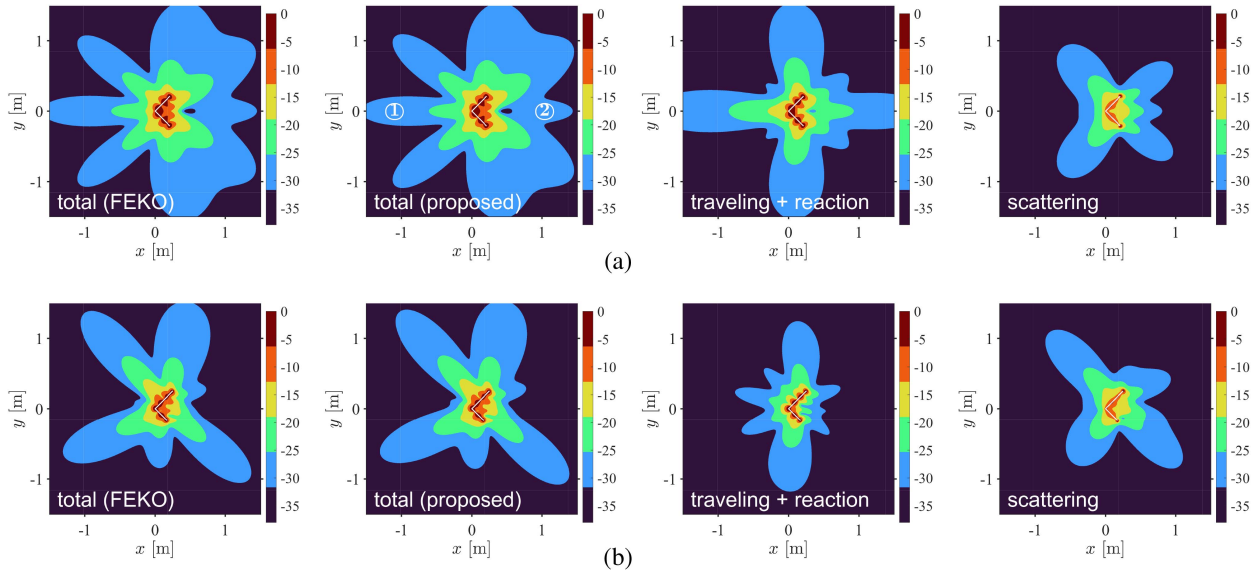


Fig. 17. Effects of the position of bend on the characteristics of field emissions. The color map displays the full-wave E-field strength in dBV/m evaluated in the  $xy$ -plane. The  $x$  and  $y$  coordinates correspond to those shown in Fig. 15 and the configurations for  $\delta = 0$  is the condition scaled to those shown in Fig. 16. As inferred from the results, the E-field accompanying the far-field lobe4 and lobe8 in Fig. 16 shrinks as the position of the bend shifts from point NQ to NI. The positions of wire structures are added using the lines in white. (a)  $\delta = 0$  (NQ). (b)  $\delta = \lambda/4$  (NI).

of  $\bar{I}_{re,\perp}$  are less simple because the field associated with the traveling wave extends in transverse dimensions, as displayed in Fig. 6. Moreover, the results suggest that this component partly complements the effect of  $E_{\parallel}$  at an acute bend. In the region wherein  $\delta$  is large, the size of the radiation reaction current shrinks owing to the short  $L_1$  compared to the transverse extension of the Sommerfeld mode.

Since the phase condition in (20) originates from the interference fringe produced by both forward- and backward-traveling waves, the aforementioned periodic properties of the position of the bend are specific to the assumption of time-harmonic fields; as for a transient phenomenon, the position of the bend will prevent the traveling pul charge's phase conditions at the bending point from being spatially periodic. However, such effects may become apparent at resonance, wherein the traveling wave dominates the entire phenomenon. Generally, this is one of the main factors that can cause a gap in characterization between the transient- and steady-state phenomena.

### C. Far-Field Characteristics

Far-field characteristics were examined by utilizing the configuration illustrated in Fig. 15, wherein an L-shaped structure of  $L_1 = L_2 = 3$  mm,  $a = 15$   $\mu$ m, and  $\gamma_1 = 90^\circ$  was excited via a plane wave in phase with  $f = 125$  GHz. The example displayed herein was selected to clearly convey the physical characteristics revealed by the model. As shown in Fig. 16, the total far-field produced by the proposed model is validated against the MoM. It can be observed that eight lobes for the total far field are present at an interval of approximately  $45^\circ$ , each of which is labeled as lobe1–lobe8. Certain traveling, reaction, and scattering components of wire units #1 and #2, as presented in Table I, characterize the dominant origin of each lobe. The lobes

TABLE I  
DOMINANT ORIGINATIONS FOR EACH FAR FIELD LOBE DISPLAYED IN FIG. 16  
BASED ON THE THREE COMPONENTS

	$\varphi$ [deg]	dominant origins of the far-field lobes
lobe1	45	scattering (#1)
lobe2	90	forward (#1), forward (#2), reaction
lobe3	135	scattering (#2)
lobe4	180	forward (#1), backward (#2), reaction
lobe5	225	scattering (#1)
lobe6	270	backward (#1), backward (#2), reaction
lobe7	315	scattering (#2)
lobe8	0	backward (#1), forward (#2), reaction

of nos. 1, 3, 5, and 7 are produced mainly by the scattering current (phenomena originating from the instantaneous scattering), and those of nos. 2, 4, 6, and 8 are caused by the currents of traveling and radiation reaction (phenomena derived from the propagation dynamics). The incident direction is chosen such that the field excites the structure for both #1 and #2 in phase, which is intended to make the far field produced by the scattering component direct the plane perpendicular to the corresponding wire units ( $\varphi = 45^\circ$  and  $225^\circ$  for #1 and  $\varphi = 135^\circ$  and  $315^\circ$  for #2). The respective lengths,  $L_1$ ,  $L_2$ , and exciting frequency,  $f$ , determine the dominant directivity of the far-field produced by the traveling and reaction components [19]. For the traveling wave, the dominant radiation directions differ between contributions from the forward- and backward-traveling waves [35], which are classified in detail in Table I. Owing to the phase relation in these components, the angles  $\varphi$ , at which the total

far field attains its maximal value, do not appear exactly every  $45^\circ$ . Although the difference in the radiation patterns by the respective components is ascribed simply to the difference in their current distributions [36], it essentially illustrates the field-line coupling dynamics predicted by the proposed model.

#### D. Field Emissions Around the Bending Point

In this section, the general expression of the E-field around the bending point is analyzed to exemplify the applicability of the proposed model to predict field emissions accompanying the antenna-mode current propagation, incorporating the radiation losses owing to the sources' dynamics.

Assuming bent wire structures with a total length  $L_1 + L_2 = 60$  cm, radius  $a = 1.5$  mm, and the exciting field of  $|\mathbf{E}| = 1$  V/m and  $f = 1.25$  GHz. These configurations were chosen such that the exciting frequency and dimensions of the example provided in Fig. 16 are scaled for a more realistic situation in EMI-related problems.

The E-field reproduced by the proposed model in the cases of different positions of bend,  $\delta = 0$  and  $\delta = \lambda/4$  is shown in Fig. 17. As shown in Fig. 17, the results of the total E-field are validated against those reproduced by MoM. Based on the presented results, the E-field varies from the near- to the far-field pattern as the observation point moves from the conductor structure (center of the color map). In particular, as the condition for  $\delta = 0$  is coordinated such that the structure and excitation are scaled to the configurations that calculated Fig. 16, the outermost contour of the color map is almost the same as the pattern shown in Fig. 16. Some of the directions in which the E-field obtains its maximal strength, as displayed by ① and ② in Fig. 17, corresponding to lobe4 and lobe8 of the far field in Fig. 16, shrinks as  $\delta$  changes from NQ to NI. As shown in Fig. 17, this trend results from the traveling and reaction characteristics. Because the EM field distributions associated with the traveling and radiation-reaction components are intrinsic to a specific wire structure and frequency, and these components properly reproduce the sensitive resonance characteristics caused by radiation losses varying depending on the structure, the model can be applied to predict the trends of the emission regardless of the distribution of the excitation.

#### V. CONCLUSION

In this study, we formulated the TL model for bent-wire structures based on the single-wire TL model reported in the literature [19]. The model integrated the mutual interaction related to radiation losses by incorporating the interaction term in the exciting E-field. The formulation was validated against the numerical results by utilizing the MoM. The reaction owing to the discontinuity at the wire ends [19] was applied to the bend points. Based on the results, we could explain the transmission and radiation characteristics corresponding to the bending points.

We clarified the physical interpretations with the longitudinal and radial components of the E-field resulting from the traveling wave on a finite-length line. The resonant characteristics, which vary depending on the bending angle, were explained using

the proposed model, based on the internal relationship between the traveling and radiation reaction components. Furthermore, the effects of the geometrical characteristics of the bent wire structure, such as the bending angle and bending position, could be understood through the analytical expression of the E-field inducing the radiation reaction.

Notably, the proposed model can be leveraged as a passive circuit element to design EM phenomena within the circuit theory, which is essential for designing antennas and metamaterials comprising wires (e.g., [26], [27], [28]). Moreover, the proposed model yields insights for solving EMI-related challenges.

#### APPENDIX A

##### EXPRESSION OF AN $N$ -UNIT SINGLE-CONDUCTOR LINE STRUCTURE IN MATRIX FORM

To simplify the formulation of bent-wire structures in Section II B, the equations provided for the respective local coordinates are combined using matrix-form expressions. The E-field is expressed with the following vector, wherein each component represents the contribution of a specific unit:

$$\hat{\mathbf{E}}(k_i) \equiv \begin{bmatrix} \hat{E}_1(k_i) \\ \vdots \\ \hat{E}_N(k_i) \end{bmatrix}. \quad (35)$$

In (35), the  $N$  units share a common wavenumber basis, which was later fixed to solve the total current in a bent structure. The total incident field is expressed as follows:

$$\hat{\mathbf{E}}(k_i) = \hat{\mathbf{E}}_{\text{ex}}(k_i) + \hat{\mathbf{E}}_{\text{tr}}(k_i) - \sum_j \hat{\mathbf{Z}}_j(k_i) \left\{ \hat{\mathbf{I}}_{\text{sc}}(k_j) + \hat{\mathbf{I}}_{\text{re}}(k_j) \right\} \quad (36)$$

where  $\hat{\mathbf{E}}_{\text{ex}}$  denotes the external field, and  $\hat{\mathbf{E}}_{\text{tr}}$  denotes the field resulting from the reaction owing to the discontinuities at the ends and bends, which is expressed as

$$\hat{\mathbf{E}}_{\text{tr}}(k_i) = \hat{\mathbf{E}}_f(k_i) + \hat{\mathbf{E}}_b(k_i) \quad (37)$$

$$\hat{\mathbf{E}}_f(k_i) = \hat{\mathbf{Z}}_f(k_i) \mathbf{I}_f(\mathbf{0}), \quad \hat{\mathbf{E}}_b(k_i) = \hat{\mathbf{Z}}_b(k_i) \mathbf{I}_b(\mathbf{L}). \quad (38)$$

$\mathbf{I}_f(\mathbf{0})$  and  $\mathbf{I}_b(\mathbf{L})$  represent the terminal values of the traveling wave, which are defined as follows:

$$\mathbf{I}_f(\mathbf{0}) \equiv \begin{bmatrix} I_{f,1}(0) \\ \vdots \\ I_{f,N}(0) \end{bmatrix}, \quad \mathbf{I}_b(\mathbf{L}) \equiv \begin{bmatrix} I_{b,1}(L_1) \\ \vdots \\ I_{b,N}(L_N) \end{bmatrix}. \quad (39)$$

The third term in (36) signifies the finite-length effect.  $\hat{\mathbf{Z}}_f(k_i)$ ,  $\hat{\mathbf{Z}}_b(k_i)$ , and  $\hat{\mathbf{Z}}_j(k_i)$  are  $N \times N$  matrices.  $\hat{\mathbf{Z}}_f(k_i)$  and  $\hat{\mathbf{Z}}_b(k_i)$  are given for each  $k_i$ , and  $\hat{\mathbf{Z}}_j(k_i)$  is given for each combination of  $k_i$  and  $k_j$ . The diagonal and off-diagonal elements of these matrices indicate the self and mutual effects, respectively. The components of  $\hat{\mathbf{Z}}_f(k_i)$  and  $\hat{\mathbf{Z}}_b(k_i)$  are obtained via Appendix B as the effect from the emitting-side unit (each column of the matrices) to the receiving one (each row of them). The components only apply the terminal values of

the traveling-wave current with an analytical function of the evaluation point relative to the terminals.

$\hat{\mathbf{Z}}_j(k_i)$  in (36) is expressed as

$$\hat{\mathbf{Z}}_j(k_i) = -\frac{(k^2 - k_j^2)Z_0}{k\hat{\chi}(k_j)}\delta_{ij}\mathbf{1}_N + \hat{\mathbf{Z}}'_j(k_i), \quad (40)$$

where  $\delta_{ij}$  denotes the Kronecker delta,  $\mathbf{1}_N$  denotes the identity matrix of size  $N$ , and  $\hat{\mathbf{Z}}'_j(k_i)$  is derived from the EM potentials (51) and (52) in Appendix C as the effect from the emitting-side unit [each column of (40)] to the receiving-side unit (each row of it). In the multiple-unit case, it is reported as a matrix form of the single-unit case (53), as shown in Appendix C. To obtain the tangential component of the E-field on the receiving-side unit, the calculation of  $\hat{\mathbf{Z}}_f(k_i)$ ,  $\hat{\mathbf{Z}}_b(k_i)$  and  $\hat{\mathbf{Z}}_j(k_i)$  requires a coordinate transformation between the local coordinate systems for the respective units.

In the wavenumber domain, the radiation reaction and scattering components in (3) are inhomogeneous solutions to (1) and are transformed into

$$\begin{aligned} & \begin{bmatrix} c\hat{\mathbf{Q}}_{sc}(k_i) \\ \hat{\mathbf{I}}_{sc}(k_i) \end{bmatrix} \\ &= \frac{\hat{\chi}(k_i)}{(k^2 - k_i^2)Z_0} \begin{bmatrix} k_i \\ k \end{bmatrix} \left\{ \hat{\mathbf{E}}_{ex}(k_i) - \sum_j \hat{\mathbf{Z}}_j(k_i)\hat{\mathbf{I}}_{sc}(k_j) \right\} \end{aligned} \quad (41)$$

$$\begin{aligned} & \begin{bmatrix} c\hat{\mathbf{Q}}_{re}(k_i) \\ \hat{\mathbf{I}}_{re}(k_i) \end{bmatrix} \\ &= \frac{\hat{\chi}(k_i)}{(k^2 - k_i^2)Z_0} \begin{bmatrix} k_i \\ k \end{bmatrix} \left\{ \hat{\mathbf{E}}_{tr}(k_i) - \sum_j \hat{\mathbf{Z}}_j(k_i)\hat{\mathbf{I}}_{re}(k_j) \right\}. \end{aligned} \quad (42)$$

As illustrated in (41) and (42), the two incident fields  $\hat{\mathbf{E}}_{ex}$  and  $\hat{\mathbf{E}}_{tr}$  correspond to the induced source variables of the scattering ( $c\hat{\mathbf{Q}}_{sc}$ ,  $\hat{\mathbf{I}}_{sc}$ ) and the radiation reaction ( $c\hat{\mathbf{Q}}_{re}$ ,  $\hat{\mathbf{I}}_{re}$ ) components, respectively. The left-hand sides of (41) and (42) are canceled by the parts originating from the first term of (40), yielding

$$\sum_j \hat{\mathbf{Z}}'_j(k_i)\hat{\mathbf{I}}_{sc}(k_j) = \hat{\mathbf{E}}_{ex}(k_i) \quad (43)$$

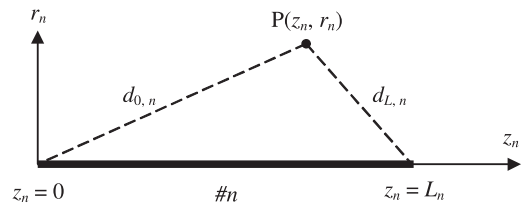


Fig. 18. Coordinates used to describe the electric fields owing to the traveling wave in  $\#n$ .

$$\sum_j \hat{\mathbf{Z}}'_j(k_i)\hat{\mathbf{I}}_{re}(k_j) = \hat{\mathbf{E}}_{tr}(k_i). \quad (44)$$

When an excitation E-field  $\hat{\mathbf{E}}_{ex}(k_i)$  is applied, all current components are expressed by  $2N$  unknown values in  $\mathbf{I}_f(0)$  and  $\mathbf{I}_b(L)$  obtained from (3), (43), and (44), which are obtained by applying Kirchhoff's current law (KCL) at the terminals in  $\#1, \dots, \#N$ .

#### APPENDIX B

##### ELECTRIC FIELD PRODUCED BY THE TRAVELING WAVE ON A FINITE-LENGTH LINE

The E-field, generated by the traveling wave propagating along a wire filament measuring  $L_n$  in length, is expressed in the local cylindrical coordinate system  $(z_n, r_n)$  as (45)–(49) shown at the bottom of this page [37], where  $d_{0,n}$  and  $d_{L,n}$  denote the distances from  $z_n = 0$  and  $z_n = L_n$  ends of unit  $\#n$  to an observation point,  $P(z_n, r_n)$  (refer to Fig. 18), and

$$G(d) \equiv \frac{e^{-jkd}}{4\pi d} \quad (50)$$

represents the free-space retarded Green's function with a distance  $d$ .

#### APPENDIX C

##### SCALAR AND VECTOR POTENTIALS GENERATED BY SOURCES OF SINGLE WAVENUMBER

For unit  $\#n$ , the Lorenz gauge scalar ( $\phi$ ) and vector ( $A_{z_n}$ ) potentials by the sources of a single wavenumber  $k_j$ , which are required to derive the finite-length effect, are expressed as

$$\phi(z_n, r_n, k_j)$$

$$E_{f,n}^{z_n}(z_n, r_n) = Z_0 \left\{ -G(d_{0,n}) + G(d_{L,n})e^{-jkL_n} \right\} I_{f,n}(0), \quad (45)$$

$$E_{f,n}^{r_n}(z_n, r_n) = \frac{Z_0}{4\pi} \left\{ \frac{e^{-jkd_{0,n}}}{r_n} \left( 1 + \frac{z_n}{d_{0,n}} \right) - \frac{e^{-jkd_{L,n}}}{r_n} \left( 1 + \frac{z_n - L_n}{d_{L,n}} \right) e^{-jkL_n} \right\} I_{f,n}(0), \quad (46)$$

$$E_{b,n}^{z_n}(z_n, r_n) = Z_0 \left\{ G(d_{0,n})e^{-jkL_n} - G(d_{L,n}) \right\} I_{b,n}(L_n), \quad (47)$$

$$E_{b,n}^{r_n}(z_n, r_n) = \frac{Z_0}{4\pi} \left\{ \frac{e^{-jkd_{0,n}}}{r_n} \left( 1 - \frac{z_n}{d_{0,n}} \right) e^{-jkL_n} - \frac{e^{-jkd_{L,n}}}{r_n} \left( 1 - \frac{z_n - L_n}{d_{L,n}} \right) \right\} I_{b,n}(L_n) \quad (48)$$

$$d_{0,n} = \sqrt{z_n^2 + r_n^2}, \quad d_{L,n} = \sqrt{(z_n - L_n)^2 + r_n^2} \quad (49)$$

$$= \frac{1}{\varepsilon_0} \int_0^{L_n} d\xi G(\sqrt{(z_n - \xi)^2 + r_n^2}) \hat{Q}(k_j) e^{-jk_j \xi} \quad (51)$$

$$A_{z_n}(z_n, r_n, k_j)$$

$$= \mu_0 \int_0^{L_n} d\xi G(\sqrt{(z_n - \xi)^2 + r_n^2}) \hat{I}(k_j) e^{-jk_j \xi} \quad (52)$$

where  $\varepsilon_0$  and  $\mu_0$  denote permittivity and permeability in free space, respectively. The respective components of scattering ( $\hat{Q}_{sc}$  and  $\hat{I}_{sc}$ ) and reaction ( $\hat{Q}_{re}$  and  $\hat{I}_{re}$ ) were applied to  $\hat{Q}$  in (51) and  $\hat{I}$  in (52). The self and mutual induction of the finite-length effect are calculated by extending its single-unit case  $\hat{Z}'_j(k_i)$ , for which

$$\begin{aligned} & \sum_i \hat{Z}'_j(k_i) e^{-jk_i z} \\ &= - \left( jk + \frac{k_j}{k} \frac{d}{dz} \right) Z_0 \int_0^L d\xi G(\sqrt{(z - \xi)^2 + a^2}) e^{-jk_j \xi}. \end{aligned} \quad (53)$$

Notably, in calculating the finite-length effect, infinite integration (because the proposed model is based on the scattering problem by infinite length lines) will be avoided similarly as in the single-unit case [see the development from (36) to (42) in [19]]. Furthermore, as the Fourier coefficients  $\hat{Z}'_j(k_i)$  that corresponds to  $\hat{Z}'_j(k_i)$  in (53) are required for the procedure, the spatial differentiation included in (53) and the same process included to obtain  $\hat{Z}'_j(k_i)$ , can be simply addressed by multiplying  $-jk_i$  as the derivative for each wavenumber component after the potential is sampled along the line.

## REFERENCES

- [1] C. R. Paul, *Analysis of Multiconductor Transmission Lines*. New York, NY, USA: Wiley-Interscience, 1994.
- [2] L. Niu and T. H. Hubing, "Rigorous derivation of imbalance difference theory for modeling radiated emission problems," *IEEE Trans. Electromagn. Compat.*, vol. 57, no. 5, pp. 1021–1026, Oct. 2015.
- [3] A. Vukicevic, F. Rachidi, M. Rubinstein, and S. V. Tkachenko, "On the evaluation of antenna-mode currents along transmission lines," *IEEE Trans. Electromagn. Compat.*, vol. 48, no. 4, pp. 693–700, Nov. 2006.
- [4] C. R. Paul, "A comparison of the contributions of common-mode and differential-mode currents in radiated emissions," *IEEE Trans. Electromagn. Compat.*, vol. 31, no. 2, pp. 189–193, May 1989.
- [5] H. Haase, T. Steinmetz, and J. Nitsch, "New propagation models for electromagnetic waves along uniform and nonuniform cables," *IEEE Trans. Electromagn. Compat.*, vol. 46, no. 3, pp. 345–352, Aug. 2004.
- [6] J. Nitsch, F. Gronwald, and G. Wollenberg, "Nonuniform transmission-line systems," in *Radiating Nonuniform Transmission-Line Systems and the Partial Element Equivalent Circuit Method*. Chichester, U.K.: Wiley, 2009, pp. 57–138.
- [7] K. K. Mei, "Theory of Maxwellian circuits," *Radio Sci. Bull.*, vol. 305, pp. 6–13, Sep. 2003.
- [8] E. Miller, "The proportionality between charge acceleration and radiation from a generic wire object," *Prog. Electromagn. Res.*, vol. 162, pp. 15–29, 2018.
- [9] Y. S. Cao, Y. Wang, L. Jiang, A. E. Ruehli, J. Fan, and J. L. Drewniak, "Quantifying EMI: A methodology for determining and qualifying radiation for practical design guidelines," *IEEE Trans. Electromagn. Compat.*, vol. 59, no. 5, pp. 1424–1432, Oct. 2017.
- [10] Y. Dou and K.-L. Wu, "Nature of antenna radiation revealed by physical circuit model," *IEEE Trans. Antennas Propag.*, vol. 69, no. 1, pp. 84–96, Jan. 2021.
- [11] J. Li, Y. Zhang, D. Liu, A. Bhoobe, J. L. Drewniak, and J. Fan, "Radiation physics from two-wire transmission line," in *Proc. IEEE Int. Symp. Electromagn. Compat.*, Santa Clara, CA, USA, 2015, pp. 160–164.
- [12] J. Li and J. Fan, "Radiation physics and design guidelines of high-speed connectors," *IEEE Trans. Electromagn. Compat.*, vol. 58, no. 4, pp. 1331–1338, Aug. 2016.
- [13] A. Sommerfeld, "Über die fortpflanzung elektrodynamischer wellen längs eines drahtes," *Annalen der Physik und Chemie*, vol. 67, pp. 233–290, 1899.
- [14] L. Rayleigh, "On the electromagnetic theory of light," *Phil. Mag.*, vol. 12, pp. 81–101, 1881.
- [15] R. G. Olsen, "On single wire power line microwave communication using low-loss modes," *IEEE Trans. Antennas Propag.*, vol. 69, no. 12, pp. 8722–8730, Dec. 2021.
- [16] H. T. Shamansky, A. K. Dominek, and L. Peters Jr., "Electromagnetic scattering by a straight thin wire," *IEEE Trans. Antennas Propag.*, vol. 37, no. 8, pp. 1019–1025, Aug. 1989.
- [17] G. S. Smith, "Teaching antenna radiation from a time-domain perspective," *Amer. J. Phys.*, vol. 69, no. 3, pp. 288–300, Mar. 2001.
- [18] G. S. Smith, "Teaching antenna reception and scattering from a time-domain perspective," *Amer. J. Phys.*, vol. 70, no. 8, pp. 829–844, Aug. 2002.
- [19] D. Tashiro, T. Hisakado, T. Matsushima, and O. Wada, "Single-conductor transmission line model incorporating radiation reaction," *IEEE Trans. Electromagn. Compat.*, vol. 63, no. 4, pp. 1065–1077, Aug. 2021.
- [20] G. Goubau, "Open wire lines," *IRE Trans. Microw. Theory Techn.*, vol. 4, no. 4, pp. 197–200, Oct. 1956.
- [21] S. Lee and M. Hayakawa, "A study on the radiation loss from a bent transmission line," *IEEE Trans. Electromagn. Compat.*, vol. 43, no. 4, pp. 618–621, Aug. 2001.
- [22] T.-I. Jeon, J. Zhang, and D. Grischkowsky, "THz sommerfeld wave propagation on a single metal wire," *Appl. Phys. Lett.*, vol. 86, Apr. 2005, Art. no. 161904.
- [23] J. Chiba, "Experimental studies of the losses and radiations due to bends in the Goubau line," *IEEE Trans. Microw. Theory Techn.*, vol. MTT-25, no. 2, pp. 94–100, Feb. 1977.
- [24] T. Akalin, A. Treizebré, and B. Bocquet, "Single-wire transmission lines at terahertz frequencies," *IEEE Trans. Microw. Theory Techn.*, vol. 54, no. 6, pp. 2762–2767, Jun. 2006.
- [25] W. K. H. Panofsky and M. Phillips, *Classical Electricity and Magnetism*, 2nd ed. Reading, MA, USA: Addison-Wesley, 1962.
- [26] O. O. Olaode, W. D. Palmer, and W. T. Joines, "Effects of meandering on dipole antenna resonant frequency," *IEEE Antennas Wireless Propag. Lett.*, vol. 11, pp. 122–125, 2012.
- [27] L. Min et al., "Electromagnetic resonance strength in metamaterials," *J. Appl. Phys.*, vol. 126, Jul. 2019, Art. no. 023103.
- [28] C. Rockstuhl, F. Lederer, C. Etrich, T. Zentgraf, J. Kuhl, and H. Giessen, "On the reinterpretation of resonances in split-ring-resonators at normal incidence," *Opt. Exp.*, vol. 14, no. 19, pp. 8827–8836, Sep. 2006.
- [29] T. Schaich, D. Molnar, A. A. Rawi, and M. Payne, "Surface wave transmission line theory for single and many wire system," *J. Appl. Phys.*, vol. 130, Nov. 2021, Art. no. 194902.
- [30] U. Paoletti, T. Suga, and H. Osaka, "Equivalent circuit for Sommerfeld wave," *IEICE Electron. Exp.*, vol. 8, no. 19, pp. 1590–1595, Oct. 2011.
- [31] J. B. Nitsch and V. Tkachenko, "Global and modal parameters in the generalized transmission-line theory and their physical meaning," *Radio Sci. Bull.*, vol. 312, pp. 21–31, Mar. 2005.
- [32] K. Wang and D. M. Mittleman, "Metal wires for terahertz wave guiding," *Nature*, vol. 432, pp. 376–379, Nov. 2004.
- [33] G. Goubau, "Surface waves and their application to transmission lines," *J. Appl. Phys.*, vol. 21, no. 11, pp. 1119–1128, Nov. 1950.
- [34] R. F. Harrington, *Time-Harmonic Electromagnetic Fields*. New York, NY, USA: McGraw-Hill, 1993.
- [35] J. D. Kraus, *ANTENNAS*, 2nd ed. New York, NY, USA: McGraw-Hill, 1988.
- [36] G. S. Smith, "On the interpretation for radiation from simple current distributions," *IEEE Antennas Propag. Mag.*, vol. 40, no. 4, pp. 39–44, Aug. 1998.
- [37] R. Lundholm, R. B. Finn, and W. S. Price, "Calculation of transmission line lightning voltages by field concepts," *AIEE Trans. Power App. Syst.*, vol. 77, pp. 1271–1283, Feb. 1958.



**Daiki Tashiro** (Member, IEEE) received the B.E. and M.E. degrees in electrical engineering from Kyoto University, Kyoto, Japan, in 2017 and 2019, respectively.

Since 2019, he has been with the Central Research Institute of Electric Power Industry (CRIEPI), Yokosuka, Japan. His current research interests include electromagnetic transient analysis of electric power facilities and modeling of electrodynamics.

Mr. Tashiro is a Member of the Institute of Electronics, Information and Communication Engineers of Japan (IEICE) and the Institute of Electrical Engineers of Japan (IEEJ).



**A. K. M. Mahfuzul Islam** (Member, IEEE) received the B.E. degree in electrical and electronic engineering, the M.E. degree in communications and computer engineering, and the Ph.D. degree in informatics from Kyoto University, Kyoto, Japan, in 2009, 2011, and 2014, respectively.

From 2013 to 2015, he was a Research Fellow with the Japan Society for the Promotion of Science. He joined the Institute of Industrial Science, University of Tokyo, Tokyo, Japan, as a Research Associate in 2015. Since 2018, he has been a Junior Associate

Professor with the Department of Electrical Engineering, Kyoto University. His research interests include low-power CMOS analog and mixed-signal circuit design, on-chip voltage regulators, and power device reliability monitoring.

Dr. Islam received the Best Paper Awards at ICMTS'2017 and ICMTS'2023, the Best Design Award at ASP-DAC'2023, and the Student Design Award at A-SSCC'2013. He received several prestigious awards, such as IPSJ Computer Science Award for Young Researchers and IEEE CEDA All Japan Joint Chapter Academic Research Award. He is a Member of IEICE and IPSJ.



**Kana Sameshima** received the B.S. degree in physics and the M.E. degree in electrical engineering from Kyoto University, Kyoto, Japan, in 2018 and 2020, respectively.



**Osami Wada** (Member, IEEE) received the B.E., M.E., and Dr. Eng. degrees in electronics from Kyoto University, Kyoto, Japan, in 1981, 1983, and 1987, respectively.

From 1988 to 2005, he was with the Faculty of Engineering, Okayama University, Okayama, Japan. From 2005 to 2023, he was a Full Professor with the Department of Electrical Engineering, Kyoto University, where he has been engaged in the study of the electromagnetic compatibility (EMC) of electronic circuits and systems, and the development of EMC

macro models of integrated circuits. After his retirement in March 2023, he joined the Center for Future Communications Research, Nagoya Institute of Technology, Nagoya, Japan, as a Visiting Professor and he is engaged in EMC evaluation of automotive Ethernet. He is currently a Professor Emeritus with Kyoto University.

Dr. Wada was the Chair of IEEE EMC Society Japan Chapter from 2012 to 2013, and the Chair of the Technical Committee of EMC (EMCJ) in the Institute of Electronics, Information and Communication Engineers of Japan (IEICE) from 2017 to 2018. He is a Fellow of IEICE, a Member of the Institute of Electrical Engineers of Japan (IEEJ) and the Japan Institute of Electronics Packaging (JIEP).



**Takashi Hisakado** (Member, IEEE) received the B.E. and M.E. degrees in electrical engineering II and the Dr. Eng. degree in electrical engineering from Kyoto University, Kyoto, Japan, in 1993, 1995, and 1997, respectively.

He is currently an Associate Professor with the Department of Electrical Engineering, Kyoto University. His research interests include the design of electromagnetic phenomena and power flows.

Dr. Hisakado is a Member of the Institute of Electronics, Information and Communication Engineers of Japan, and the Institute of Electrical Engineers of Japan.